ADVANCED ENERGY MATERIALS
www.advenergymat.de

# Exploring the Thermal and Ionic Transport of $Cu^+$ Conducting Argyrodite $Cu_7PSe_6$

*Anupama Ghata, Tim Bernges, Oliver Maus, Björn Wankmiller, Aakash Ashok Naik, Joana Bustamante, Michael W. Gaultois, Olivier Delaire, Michael Ryan Hansen, Janine George, and Wolfgang G. Zeier**

**Understanding the origin of low thermal conductivities in ionic conductors is essential for improving their thermoelectric efficiency, although accompanying high ionic conduction may present challenges for maintaining thermoelectric device integrity. This study investigates the thermal and ionic transport in $Cu_7PSe_6$, aiming to elucidate their fundamental origins and correlation with the structural and dynamic properties. Through a comprehensive approach including various characterization techniques and computational analyses, it is demonstrated that the low thermal conductivity in $Cu_7PSe_6$ arises from structural complexity, variations in bond strengths, and high lattice anharmonicity, leading to pronounced diffuson transport of heat and fast ionic conduction. It is found that upon increasing the temperature, the ionic conductivity increases significantly in $Cu_7PSe_6$, whereas the thermal conductivity remains nearly constant, revealing no direct correlation between ionic and thermal transport. This absence of direct influence suggests innovative design strategies in thermoelectric applications to enhance stability by diminishing ionic conduction, while maintaining low thermal conductivity, thereby linking the domains of solid-state ionics and thermoelectrics. Thus, this study attempts to clarify the fundamental principles governing thermal and ionic transport in $Cu^+$-superionic conductors, similar to recent findings in $Ag^+$ argyrodites.**

## 1. Introduction

The ultralow lattice thermal conductivity in superionic conductors plays a pivotal role in energy conversion technology, fuel cells, and various thermoelectric applications.[1–4] In ionic conductors, the role of fast ionic diffusion in the frequently observed low lattice thermal conductivity remains elusive.[5] However, recent studies of the material class of ion-conducting argyrodites suggest that their low thermal conductivity originates from structural disorder, weak bonding of mobile ions, and high lattice anharmonicity, rather than the diffusion of mobile ions.[6,7] Understanding the origin of low lattice thermal conductivity by testing the relationship of transport with lattice dynamics and structure is of fundamental importance as it can reveal guidelines and design principles for the development and discovery of material classes.[8,9]

In the past, the thermal transport of crystalline thermoelectric materials has

A. Ghata, T. Bernges, O. Maus, W. G. Zeier
Institute of Inorganic and Analytical Chemistry
University of Münster
D-48149 Münster, Germany
E-mail: wzeier@uni-muenster.de

O. Maus, B. Wankmiller, M. R. Hansen, W. G. Zeier
International Graduate School for Battery Chemistry
Characterization
Analysis
Recycling and Application (BACCARA)
University of Münster
D-48149 Münster, Germany

The ORCID identification number(s) for the author(s) of this article can be found under https://doi.org/10.1002/aenm.202402039



**DOI: 10.1002/aenm.202402039**

B. Wankmiller, M. R. Hansen
Institute of Physical Chemistry
University of Münster
D-48149 Münster, Germany

A. A. Naik, J. Bustamante, J. George
Federal Institute for Materials Research and Testing (BAM)
D-12205 Berlin, Germany

A. A. Naik, J. George
Institute of Condensed Matter Theory and Solid-State Optics
Friedrich Schiller University
07743 Jena, Germany

M. W. Gaultois
Leverhulme Research Centre for Functional Materials Design
Department of Chemistry
University of Liverpool
51 Oxford Road, Liverpool L7 3NY, UK

O. Delaire
Department of Mechanical Engineering and Materials Science
Duke University
Durham, NC 27708, USA

primarily been described by the phonon-gas model, envisaging phonons as quasiparticles that propagate over length scales significantly exceeding interatomic distances.[9,10] From this phonon-gas viewpoint, several factors such as point defects,[11] anharmonicity,[5] variations in bond strengths,[12] as well as lattice complexity,[9] can suppress the propagation of these phonon quasiparticles (also called propagons) by inducing scattering.[8] Frequent scattering events lead to a reduction of the propagon mean-free paths and subsequently, a lowering of the lattice thermal conductivity.

However, complex crystalline materials have been reported with low thermal conductivities that cannot be explained by only considering gas-like heat transport by propagating phonons.[8] In these cases, the magnitude of thermal conductivity is so low that the phonon mean-free paths would have to be comparable to or even shorter than the interatomic distances, thereby making the phonon wavevector no longer well-defined.[13] This lower limit of thermal conductivity in the phonon-gas model is commonly associated with amorphous materials (i.e., the so-called glass-limit).[13] However, it has been observed to be diminished in complex crystalline materials such as $Tl_3VSe_4$,[14] $Yb_{14}MnSb_{11}$,[8] $La_2Zr_2O_7$,[15] $BaAg_2Te_2$,[16] $CuBiSeCl_2$,[17] and the aforementioned Ag argyrodites.[6]

Following this observation, a different mechanism of heat transport was proposed, characterized by a diffusive, random exchange of thermal energy between phonon modes on a local scale (i.e., by so-called diffusons) that can describe thermal conductivities below the lower limit associated with phonon-gas transport.[6,18] This distinct transport mechanism arises from the overlap of phonon modes that are close in frequency and substantially broadened, e.g., through anharmonicity, leading to the transfer of thermal energy between the modes. For example, in $Tl_3VSe_4$, strong anharmonicities and low phonon group velocities, all of which suppress phonon-gas transport by quasilocalization in real space, result in strong phonon coupling and significant diffuson contributions.[14] These dynamic characteristics are attributed to the weak bonding of heavy $Tl^+$ ions that scatter propagating phonons and facilitate low-frequency, low-velocity phonon modes with short mean-free paths, making them prone to exhibiting diffuson character.[14] By contrast, Xia et al. recently proposed a particle-like propagation of phonon excitation considering existing, but minor contributions from the off-diagonal terms of the heat-current operator to describe successfully the experimentally obtained low thermal conductivity in $Tl_3VSe_4$.[19] Similarly, $Yb_{14}MnSb_{11}$ shows strong diffuson contributions related to structural complexity, leading to a high density of phonon modes (in energy space), such that little broadening is sufficient for mode coupling.[8]

In the $Ag^+$ conducting argyrodites, the diffuson contributions dominate over propagating phonon transport at room temperature.[6] Again, this is thought to be related to strong anharmonicity, structural complexity, and a large number of low-frequency, low-velocity phonons originating from weak $Ag^+$ bonding.[6] Thus far, it remains unknown if the predominance of diffuson transport extends to the $Cu^+$ conducting argyrodites. In addition, the interrelation between ionic and thermal transport was tested in the silver argyrodites and no direct relation was found.[6] However, a similar study discussing both transport properties in comparison is missing in the $Cu^+$-based argyrodites.

The present work seeks to shed light on the mechanism of thermal transport and its relation to the structural and dynamic character of $Cu_7PSe_6$. To achieve these objectives, a combination of characterization techniques is employed, including temperature-dependent X-ray diffraction and pair-distribution function analysis, nuclear magnetic resonance spectroscopy, impedance spectroscopy, as well as thermal transport measurements. To corroborate the experimental results, lattice dynamics computations, crystal orbital Hamilton population (COHP) analyses, bond-valence sums, and analytical modeling of thermal transport were conducted. With that, this study demonstrates the strong variations of bond strengths, structural complexity, and high lattice anharmonicity that lead to diffuson transport of heat and facilitate fast ionic conduction.

## 2. Results and Discussion

### 2.1. Crystal Structure and Phase Analysis

$Cu_7PSe_6$ is known to undergo multiple phase transitions in the investigated temperature regime.[20,21] Consequently, temperature-dependent Bragg diffraction was conducted as initial characterization of all phases. The waterfall plot of the corresponding diffraction pattern (**Figure 1a**) shows the expected two-phase transitions in $Cu_7PSe_6$, occurring below 250 and above 320 K.[20,21] Below 250 K, the material crystallizes in an orthorhombic phase (space group $Pna2_1$) that is characterized by a fully ordered (occupied) substructure of $Cu^+$ ions coordinated by $Se^{2-}$ ions (Figure S1a, Supporting Information). The $Cu^+$ ions reside in four types of $Se^{2-}$ coordination environments: trigonal planar, triangular noncoplanar, linear, and tetrahedral (Figure S1b, Supporting Information). Vice versa, $Se^{2-}$ is either fully coordinated by $Cu^+$ or part of rigid $PSe_4^{3-}$ units. Above 250 K, $Cu_7PSe_6$ crystallizes in a cubic phase with a space group $P2_13$ composed again, of a rigid framework of $PSe_4^{3-}$ tetrahedra.[21] Within this phase, the $Cu^+$ ions are located in four distinct positions either fully or partially occupied (Figure S1c, Supporting Information),[21] and coordinated either triangularly, tetrahedrally, or linearly by $Se^{2-}$ ions (Figure S1d, Supporting Information). Upon further increase of the temperature to 320 K, $Cu_7PSe_6$ transitions into a high-temperature cubic phase (space group $F\bar{4}3m$), where $Cu^+$ ions are partially

O. Delaire
Department of Chemistry
Duke University
Durham, NC 27708, USA
O. Delaire
Department of Physics
Duke University
Durham, NC 27708, USA
W. G. Zeier
Institut für Energie- und Klimaforschung (IEK)
IEK-12: Helmholtz-Institut Münster
Forschungszentrum Jülich
48149 Münster, Germany

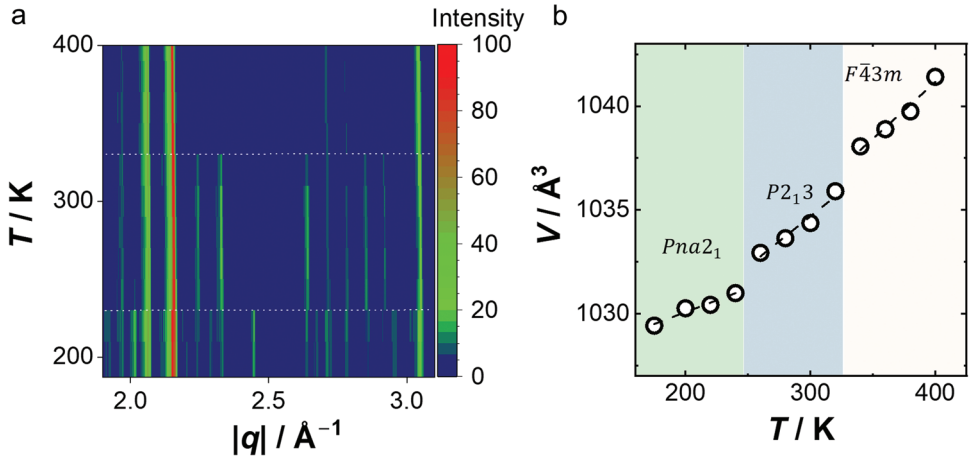


**Figure 1.** a) Heatmap of temperature-dependent X-ray diffraction of $Cu_7PSe_6$ from 175 to 400 K. Intensity information is color-coded, from blue (low intensity) to red (high intensity). The intensity of reflections indicates two phase transitions of $Cu_7PSe_6$ at below 250 and above 320 K (highlighted by dashed lines). b) Unit cell volume as a function of temperature. The color shaded regions indicate the temperature range of the different phases.

occupying three sites, with three distinct $Se^{2-}$ positions either as part of the tetrahedral $PSe_4^{3-}$ unit or fully coordinated by $Cu^+$ (Figure S1e, Supporting Information).[21] In this phase, the $Cu^+$ substructure can be described by cage-like frameworks of $Cu^+$, where each $Cu^+$ site is tetrahedrally or triangularly coordinated by $Se^{2-}$ (Figure S1f, Supporting Information).[22] The large number of available $Cu^+$ positions, together with their partial occupation, is often discussed as the origin of the high ionic conductivities observed in the ($Li^+$, $Cu^+$, $Ag^+$)-argyrodite material class.[6,23,24]

Pawley refinements were performed for all diffractograms, confirming the expected phases and showing the expected linear increase of the unit cell volumes with temperature (Figure 1b). Shaded regions indicate the temperature range in which the respective phases were observed. The linear increase of the unit cell volumes for each phase was used to calculate the volumetric thermal expansion coefficients, which are $7.3 \pm 0.4 \times 10^{-6}$, $15.5 \pm 1.0 \times 10^{-6}$, and $17.5 \pm 1.0 \times 10^{-6}$ $K^{-1}$ for the phases with space groups $Pna2_1$, $P2_13$, and $F\bar{4}3m$, respectively. Rietveld refinements were conducted on prolonged diffraction measurements for each phase at representative temperatures to extract additional structural information (see Section S4 in the Supporting Information).

In addition to Bragg diffraction, pair-distribution function analyses were conducted at three different temperatures to test the agreement between average and local structure in $Cu_7PSe_6$ (results shown in Section S6 in the Supporting Information). These analyses corroborate the refined structural parameters for each phase that were previously determined through Bragg diffraction and shows no signs of symmetry reduction on the local scale (details in Section S6 in the Supporting Information).

The extracted structural parameters from refinements of both, Bragg diffraction and pair-distribution function data, illustrate a strong increase of the isotropic thermal displacement parameter ($u_{eq}$) of $Cu^+$ from $0.021 \pm 0.001$ to $0.067 \pm 0.003$ $Å^2$ upon increasing the temperature from 200 to 400 K. The higher magnitude of the thermal displacements of $Cu^+$ ions and their strong increase with temperature indicate weak bonding and high mobility of $Cu^+$ in the structures. To evaluate the bonding characteristics in more detail, the bonding and antibonding states within the electronic structure are analyzed using COHPs of the low-temperature orthorhombic phase (details provided in Section S7 in the Supporting Information). Despite the disorder on $Cu^+$ sites in both the intermediate-temperature cubic ($P2_13$) and the high-temperature cubic ($F\bar{4}3m$) phases, the comparable coordination geometry to the low-temperature orthorhombic ($Pna2_1$) phase suggests similar bonding trends. To test this hypothesis, a simplistic model for the intermediate-temperature cubic ($P2_13$) phase is built (details in Section S7 in the Supporting Information), excluding the high-temperature cubic ($F\bar{4}3m$) phase due to the lack of a suitable structural model. While various distinct Cu–Se bonds can be identified in the low-temperature orthorhombic ($Pna2_1$) phase, they all demonstrate similar bonding characteristics, quantified by integrated populations between −0.98 and −1.53 eV with an average and standard deviation of −1.24 ± 0.17 eV between all seven distinct types of bonds (Table S8, Supporting Information). Additionally, all Cu–Se bonds are characterized by occupied antibonding states below the Fermi level, which leads to ≈25% antibonding contributions in average overall bonds (Table S8, Supporting Information). The summed up COHPs for all Cu–Se bonds are shown in **Figure** 2a, while the results for all distinct types of bonds are provided in Section S7 (Supporting Information). The low integrated populations and the significant antibonding contributions highlight the weak bonding of $Cu^+$ within the structure that is a foundation for fast $Cu^+$ transport. Furthermore, the significant fraction of occupied antibonding states below the Fermi level can facilitate anharmonicity of the Cu–Se bonds and their corresponding vibrations, suggesting a significant impact on thermal transport.[25] In contradistinction, the P–Se bond exhibits significantly stronger bonding characteristics quantified by a higher integrated population of −4.65 eV with only small antibonding interactions (≈7%) below the Fermi level (Figure 2a and Table S8 (Supporting Information)). Similar bonding–antibonding characteristics for the Cu–Se and P–Se bonds are also observed in the model of the intermediate-temperature cubic ($P2_13$) phase (Figure S8 and

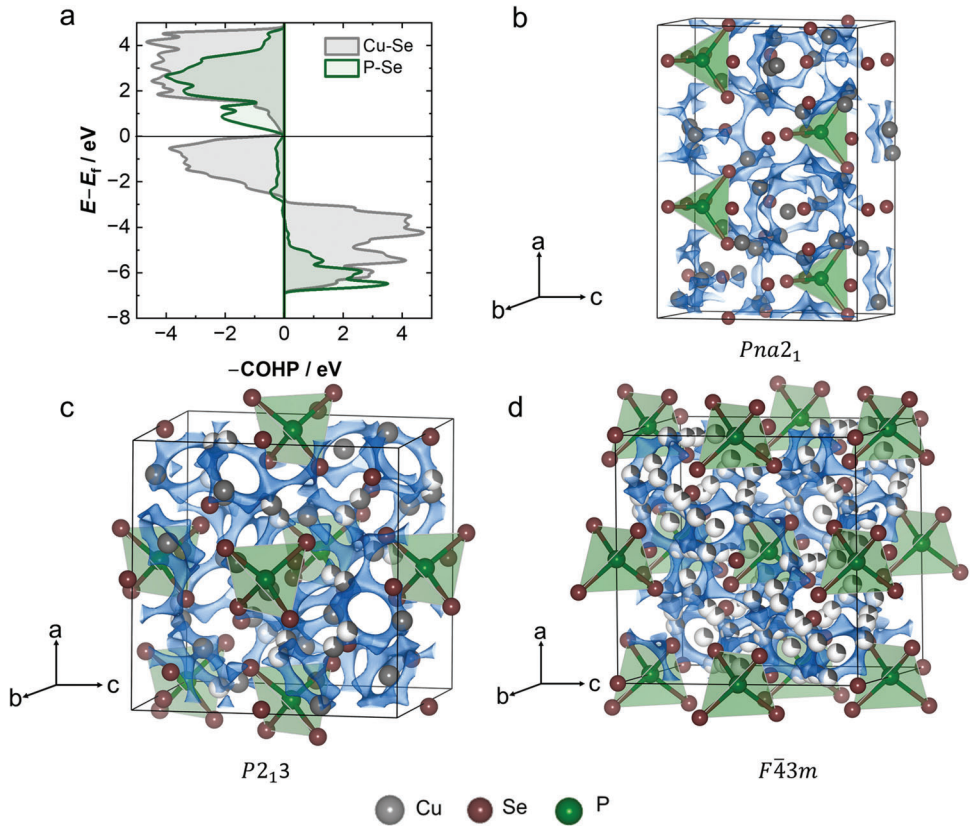


**Figure 2.** a) The comparison of summed crystal orbital Hamilton populations for Cu–Se bonds with that of P–Se bonds in the $PSe_4^{3-}$ unit reveals a strong difference in bonding interactions. b–d) Bond-valence sum energy landscapes of $Cu_7PSe_6$ illustrating all potential $Cu^+$ 3D diffusion pathways within the various phases. Gray, green, and maroon colors represent $Cu^+$, P, and $Se^{2-}$, respectively, with the blue isosurface indicating bond valance of site energy of $Cu^+$ ions.

Table S9, Supporting Information) (details provided in Section S7 in the Supporting Information).

The significantly weaker bonding of $Cu^+$ indicated by the COHP analysis is in agreement with the high thermal displacement parameters of $Cu^+$ observed in the structural analyses (and their stronger increase with temperature). In comparison, the thermal displacement of the stronger bonded $Se^{2-}$ (in the $PSe_4^{3-}$ rigid unit) changes only marginally with temperature (details in Section S4 in the Supporting Information). In addition to the COHP analysis, bond-valence sum energy[26] isosurfaces of $Cu^+$ in $Cu_7PSe_6$ were calculated, that reveal a highly connected, 3D diffusion network for $Cu^+$ in all three phases (Figure 2b–d). This high degree of connectivity, together with the weak overall covalency of $Cu^+$, can be considered the prerequisite for fast ion conduction, not exclusive to the high temperature phase.

In conclusion, the structural investigations confirm the reported phase transitions that lead to a change of the $Cu^+$ substructure, while the rigid $PSe_4^{3-}$ bonding environment persists. Moreover, bonding analyses by COHP confirm the expected strong bonding characteristics of the rigid framework, i.e., the $PSe_4^{3-}$ units, while emphasizing the weak bonding of $Cu^+$ in $Cu_7PSe_6$. This weak bonding, characterized by both, a low population of bonding states and significant antibonding contributions, can be considered to facilitate ion mobility in the $Cu^+$ argyrodites.

### 2.2. $Cu^+$-Ion Transport

Nuclear magnetic resonance (NMR) and impedance spectroscopy experiments were conducted to evaluate the magnitude and temperature dependence of ionic transport in $Cu_7PSe_6$. To elucidate the $Cu^+$-ion dynamics from NMR spectroscopy, static lineshape analysis, and spin–lattice relaxometry experiments were performed on the isotopes $^{63}Cu$ and $^{65}Cu$ between 323 and 441 K.[27] Consequently, the ion dynamics in the high-temperature phase with space group $F\bar{4}3m$ were evaluated.

The $T_1$-relaxation rates for both isotopes, as obtained from spin–lattice relaxometry are shown in **Figure 3**a. Only the high temperature flank of the relaxation rate curve is observed, allowing a straightforward determination of the activation barrier for $Cu^+$ diffusion (0.173 ± 0.001 and 0.169 ± 0.001 eV for $^{63}Cu$ and $^{65}Cu$, respectively). The analysis of the static temperature-dependent linewidth broadening confirms the results of the $T_1$-relaxation experiments (presented in Figure S9 in the Supporting Information). With that, the determined activation barriers are in good agreement with literature reports of 0.15 eV for the high-temperature ionic conductivity of $Cu_7PSe_6$ (literature values illustrated in Figure 3b).[28] The $Cu^+$ transport characterization by NMR is limited to the high-temperature phase ($F\bar{4}3m$ space group), beyond 320 K, in this study. The corresponding characterization for the lower temperature phases could not

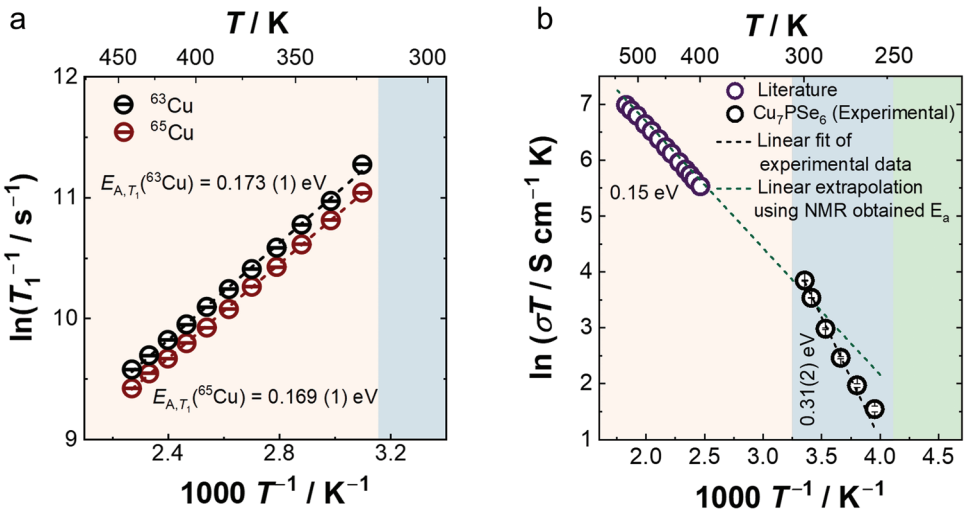


**Figure 3.** a) Arrhenius plots of the spin–lattice relaxation rates $T_1^{-1}$ for $^{63}$Cu and $^{65}$Cu determined from NMR spectroscopy. b) Comparison of activation energy barrier of $Cu_7PSe_6$ in different temperature regions. Literature data[28] of the high temperature ionic conductivities are linearly extrapolated (green dashed line) to the lower temperature, where the slope of the line represents the activation barrier determined by NMR spectroscopy. This extrapolation aligns with the highest conductivity value measured experimentally via impedance spectroscopy (represented by black data points) confirming the coherence of the results.

be conducted due to strong quadrupolar broadening hindering the evaluation of the $^{63}$Cu/$^{65}$Cu NMR signals.[27] Additionally, temperature-dependent $^{31}$P magic angle-spinning and $^{77}$Se static NMR experiments were performed, corroborating the observed high-temperature phase transition in $Cu_7PSe_6$, as discussed in Section S9 (Supporting Information). To overcome the limitation of NMR experiments for the lower temperature phases, impedance spectroscopy experiments were conducted on the intermediate temperature phase (space group $P2_13$, between 253 and 298 K). Analyses of the impedance data (Figure S13, Supporting Information) demonstrate that the fast ionic transport of the high-temperature phase, shown in literature and confirmed by NMR experiments, persists to the intermediate temperature phase with a room-temperature conductivity of 127 ± 23 mS cm$^{-1}$ (±18%, standard deviation from four measurements). The structural transition to the intermediate temperature phase (Figure S1, Supporting Information) leads to an increase in the activation energy to 0.31 ± 0.02 eV. Details of the experimental procedure can be found in Section S10 (Supporting Information). Analogous characterization of the lowest temperature phase (space group $Pna2_1$) was not possible due to experimental constraints; below 250 K, $Cu_7PSe_6$ undergoes a phase transition, causing the impedance spectrum to become highly scattered and impossible to analyze reliably.

To compare the ionic conductivities obtained from impedance spectroscopy with diffusion coefficients reported in the literature,[22] the Nernst–Einstein equation is used with a Haven ratio of unity and the number density of $Cu^+$ in the structure as carrier density in the first approximation. With that, the room-temperature $Cu^+$ diffusivity can be approximated as 0.81 × 10$^{-6}$ cm$^2$ s$^{-1}$ in good agreement with the results of machine-learned molecular dynamics simulations reported by Gupta et al. (0.8 × 10$^{-6}$ cm$^2$ s$^{-1}$ at 300 K),[22] thereby corroborating our experimental findings. Further confirmation of the consistency of the experimental results can be shown by the good agreement of all data when extrapolating the reported high-temperature conductivities to lower temperatures using the activation energy determined by NMR spectroscopy (green dashed line in Figure 3b).

Fast $Cu^+$-ionic transport is found in both, the high- and intermediate-temperature phases. While structural changes during the phase transition lead to a change of the activation energy for ionic transport, the weak overall bonding, also present in the lowest temperature phase as indicated by COHP analysis, persists and allows for fast $Cu^+$ diffusion. With that, $Cu^+$ can be considered at least partially mobile in all phases of $Cu_7PSe_6$.

### 2.3. Density of States and Heat Capacity

Following the investigation of the structure- and temperature-dependent ionic transport, the lattice dynamics are characterized to understand the origin of the reported low thermal conductivity of $Cu_7PSe_6$. In a recent study by Gupta et al.,[22] the temperature-dependent phonon density of states in $Cu_7PSe_6$ was investigated using both inelastic neutron scattering and machine-learned molecular dynamics simulations.[22] The reported computational results are presented again in **Figure** 4a. Analyzing the atom-specific contributions to the calculated total phonon density of states, it becomes evident that most phonon modes within the low-frequency spectrum (<3 THz), are associated with $Cu^+$ vibrations. This is in line with the weak bonding of $Cu^+$ shown by our COHP analysis suggesting low force constants (low frequencies) and in agreement with results of our own quasiharmonic lattice dynamics calculations on the low-temperature orthorhombic ($Pna2_1$) phase (details in Section S11 in the Supporting Information). The densities of state exhibit significant peak broadening with increasing temperature that can partly be explained by the phase transitions that increase the number of phonon modes and thus lead to a higher density of modes in energy space, and

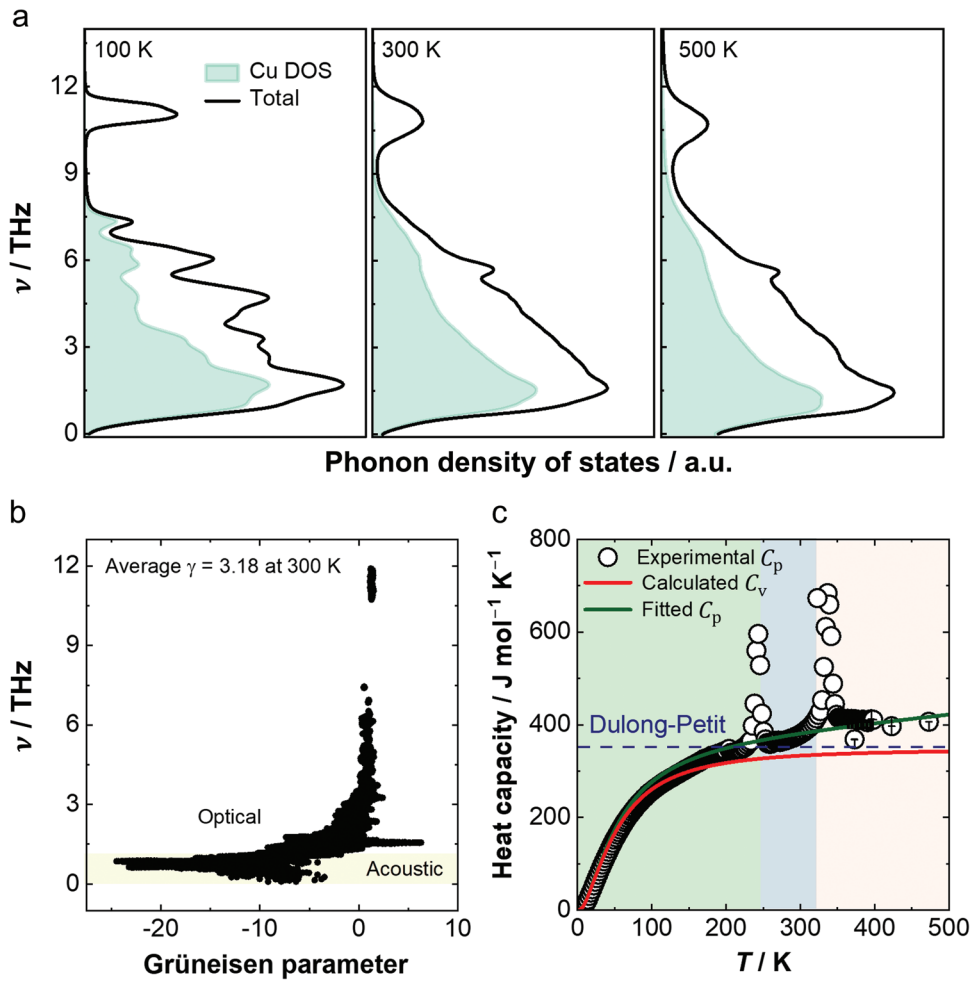


**Figure 4.** a) Calculated total and Cu atom projected phonon density of states of $Cu_7PSe_6$ at three different temperatures: 100, 300, and 500 K. b) Representation of Grüneisen parameter as a function of frequency. c) Comparison of measured heat capacity (black data points) with the theoretical heat capacity at constant volume ($C_v$) calculated from the phonon density of states (red line). In addition, a dilation term was introduced to calculate ($C_p$) values and fit the experimental results (green line).

with increased scattering that smears out the phonon branches in energy.

To gain a further understanding of this trend with temperature, spectral Grüneisen parameters were calculated based on our quasiharmonic calculations (details in Section S11 in the Supporting Information). The spectral Grüneisen parameters demonstrate highly anharmonic vibrations (i.e., high Grüneisen parameters), especially pronounced by a large peak in the low frequency (≈1.3 THz), $Cu^+$ vibration dominated, regime (Figure 4b). This strong anharmonicity is expected to substantially contribute to phonon linewidth broadening (i.e., linewidths of phonon branches become large enough to overlap the phonon modes in energy space) with increasing temperature, thus facilitating the observed merging of peaks in the density of states.[8] The large anharmonicity in the ion-conducting $Cu_7PSe_6$ is in line with prior works on superionic conductors such as $Na_3PS_4$,[29] $AgCrSe_2$,[5] $CuCrSe_2$,[30] and $Ag_8MSe_6$ ($M$ = Si, Ge, Sn),[6] where similar low-frequency peaks in anharmonicity, corresponding to mobile ion vibrations, were observed. This indicates that anharmonicity plays an overarching, general role in achieving high ionic conductivities. Moreover, from a thermal transport perspective, anharmonicities are known to induce strong phonon scattering, thereby suppressing phonon-gas transport. Dominated by the peak at low frequency, a high macroscopic Grüneisen parameter of 3.18 at 300 K is estimated for $Cu_7PSe_6$. This analysis does not only confirm the dominance of mobile ion vibrations at very low frequencies but also the presence of pronounced anharmonicity in $Cu_7PSe_6$ in agreement with the results for their $Ag^+$ conducting counterparts.[31] The strong anharmonicity of the $Cu^+$ vibrations can be understood by considering the high fraction of occupied, antibonding states (Figure 2a), emphasizing the weak bonding situation of $Cu^+$ within the structure,[25] that in turn leads to fast transport and anharmonic vibrations.[31]

In addition to the computational study of the phonon distribution and anharmonicity, the isobaric heat capacity ($C_p$) of $Cu_7PSe_6$ was determined experimentally within the temperature range of 2–500 K (Figure 4c). In agreement with our temperature-dependent X-ray diffraction analysis, two-phase transitions are observed in the heat capacity measurements (peaks at 250 and 320 K).

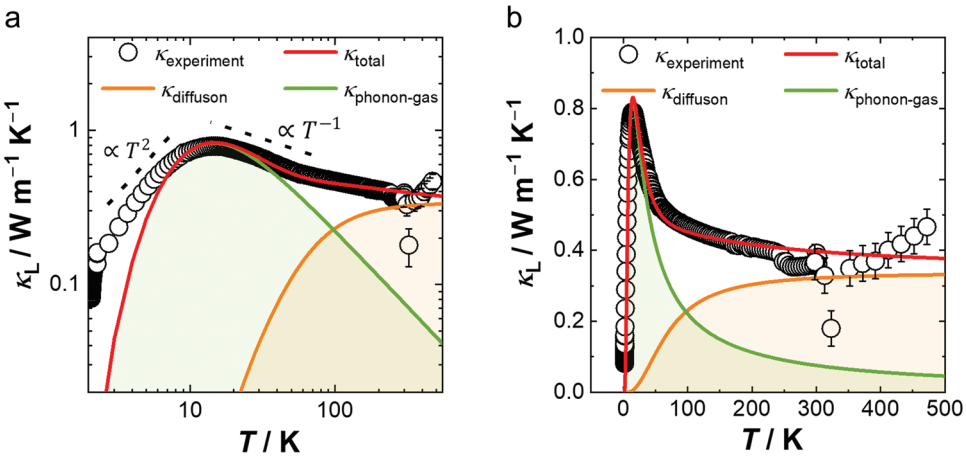


**Figure 5.** Representation of lattice thermal conductivity with temperature in $Cu_7PSe_6$. a) A logarithmic plot that emphasizes specific relationships within the thermal conductivity data, providing insights into the complex interplay of transport mechanisms. b) Two-channel analytical model of experimental lattice thermal conductivity from 2 to 500 K. This plot illustrates the distinct contributions to total lattice thermal conductivity, with the phonon-gas contributions depicted in the green shade and the diffuson-type thermal transport highlighted in the orange shade.

The increase in heat capacity at the phase transition temperatures signifies a change in the entropy of the system, driving the transformation between two different crystal structures.[32] To corroborate our experimental results, first, the heat capacity at a constant volume ($C_v$) is calculated based on the calculated phonon density of states as follows[33]

$$C_v = 3nk_B \int_0^\infty \left(\frac{g(\omega)}{3n}\right)\left(\frac{\hbar\omega}{k_B T}\right)^2 \left(e^{\frac{\hbar\omega}{k_B T}}\right)\left(e^{\frac{\hbar\omega}{k_B T}} - 1\right)^{-2} d\omega \quad (1)$$

where $n$ denotes the number density of atoms, $(\frac{g(\omega)}{3n})$ represents the normalized density of states, and $\omega$ is the angular phonon frequency ($\omega = 2\pi\nu$).

At low temperatures (<200 K), the isobaric experimental data show good agreement with the calculated isochoric values. However, at higher temperatures (>200 K), there is a noticeable difference between both. This difference can generally be assigned to the dilation term, relating the isochoric to the isobaric heat capacity, following[33]

$$C_p = C_v + B\alpha_v^2 T \quad (2)$$

where $B$ is the isothermal bulk modulus, $\alpha_v$ is the volumetric thermal expansion coefficient, and $T$ is the absolute temperature. By fitting the experimental data, excluding the peaks at phase transition temperatures with Equation (2), $\alpha_v = 17.5 \times 10^{-6}$ K$^{-1}$ as determined from temperature-dependent Bragg diffraction, and $B$ as a variable for fitting, the linear increase at high temperatures can be described accurately. The best fit to the experimental results is achieved for $B \approx 4$ GPa. To easily assess the fitting of the experimental data at low-temperature regions (<50 K) a lin–log plot is shown in Figure S20b (Supporting Information).

Having explored the phonon density of states, heat capacity, and inherent anharmonicity of the system, it is essential to consider how these characteristics influence thermal transport. Especially, strong anharmonicity can play a crucial role as a driving force for phonon–phonon scattering and by enabling diffuson-type mode coupling and diffuson transport.[6,8,34]

### 2.4. Thermal Transport

The lattice thermal conductivity of $Cu_7PSe_6$ is assessed across a large temperature range to gain insights into the underlying mechanisms of heat conduction. The lattice thermal conductivity ($\kappa_L$) is obtained by subtracting the partial electronic thermal conductivity ($\kappa_e$) from the total measured thermal conductivity ($\kappa_{tot}$).[35] Seebeck coefficient ($S$) values were utilized to calculate Lorenz number ($L$, Equation (S4), Supporting Information). Details and depictions of both, the total and electronic thermal conductivity can be found in Section S14 (Supporting Information).

The obtained lattice thermal conductivity of $Cu_7PSe_6$ from 2 to 500 K is shown in **Figure 5a**. At the lowest temperatures, from 2 to 12 K, the thermal conductivity follows $a \propto T^2$ dependence, indicating the presence of frequency-dependent boundary scattering.[10] With increasing temperature (12–100 K), the conductivity starts to decrease inversely proportional to the temperature ($\propto T^{-1}$), a signature of Umklapp (phonon–phonon) scattering.[10] The transition between the dominant boundary and phonon–phonon scattering around 12 K concludes a characteristic thermal conductivity peak.[36] At elevated temperatures (between 100 and 300 K), the thermal conductivity remains relatively unchanged with temperature.

Generally, this can be related to the high temperature limit of propagon transport or by considering diffuson transport, as tested later.[13,18] In this regime (>100 K), the experimentally obtained lattice thermal conductivity falls below the theoretical "minimum" thermal conductivity ($\kappa_{min} = 0.49$ W m$^{-1}$ K$^{-1}$) expected from a phonon-gas model perspective (calculated according to Cahill et al.).[13] This "minimum" conductivity represents the Ioffe–Regel limit given by the critical condition in which the phonon mean-free path becomes comparable to the phonon wavelength.[18,37] At this point, phonons are expected to lose their wave-like properties, leading to a drastic change in the transport properties.[18,21]

To evaluate if diffuson contributions arise as a consequence of this mean-free path limit, an analytical two-channel model, accounting for both transport mechanisms, is used to fit the

experimental results. In the model, the total lattice thermal conductivity is expressed as[8,38]

$$\kappa_L = \kappa_{phonon-gas} + \kappa_{diffuson} \quad (3)$$

where a transition frequency is introduced and utilized to separate the phonon density of states into regimes that contribute to each of the transport channels.[10] In this work, the cutoff frequency of the acoustic phonons (≈1.3 THz), coinciding with the large peak in the Grüneisen parameter, is utilized as transition frequency, as it is expected that such large anharmonicity facilitates the breakdown of the phonon wave character (i.e., the transition from classical phonon to diffuson transport of heat) and given that most optical modes have negligible group velocities (Figure S18, Supporting Information). After establishing the transition frequency, the experimental data are fitted using phonon–phonon and boundary scattering rates to describe $\kappa_{phonon-gas}$ within the phonon gas model, and a coupling probability of diffusons to describe $\kappa_{diffuson}$.[8,10,38] In addition to these fitting parameters, the calculated phonon density of states is utilized to describe the frequency distribution and heat capacity evolution within the model. A detailed discussion of the modeling procedure and the obtained fit parameters can be found in Section S15 (Supporting Information).

The resulting model describes the experimental lattice thermal conductivities of $Cu_7PSe_6$ with high accuracy (Figure 5b). The model reveals that the thermal conductivity at the lowest temperatures (<100 K) shows phonon-gas-like behavior with a well-defined peak that gradually decreases with an increase in temperature due to phonon–phonon scattering. With that, in the temperature range from 5 to 100 K, phonon-gas-like heat transport is predominant. However, above 100 K, diffuson-mediated transport becomes dominant, accounting for ≈80% of total thermal conductivity at 300 K and being responsible for the overall low magnitude and temperature-independent conductivities. The strong presence of diffuson-like transport at high temperatures can be understood based on the large number of phonon modes and their close energetic proximity (Figure S19, Supporting Information), together with the strong anharmonicity (Figure 4b), leading to spatial localization of phonons and their coupling, meaning their overlap in energy space. Nonetheless, at lower temperatures, where less phonons are occupied and scattering is limited, phonon-gas transport prevails. This result is in agreement with two-channel considerations of the Ag argyrodites,[6,38] as well as other complex crystalline materials, e.g., $Tl_3VSe_4$,[14] $Yb_{14}MnSb_{11}$,[8] and $CuBiSeCl_2$.[17]

### 2.5. Correlation between Ionic and Thermal Transport

No direct relation between ionic and thermal transport was observed in this study. On the one hand, the ionic conductivity exhibits a strong increase with temperature from 15.8 mS cm$^{-1}$ (determined here) to ≈1200 mS cm$^{-1}$ (taken from literature),[28] representing an absolute increase of about two orders of magnitude (**Figure 6**). This increase is expected from the Arrhenius relation for ionic transport, and emphasized by changes in the activation energy from 0.31 to 0.15 eV as a consequence of the high-temperature phase transition. On the other hand, the thermal

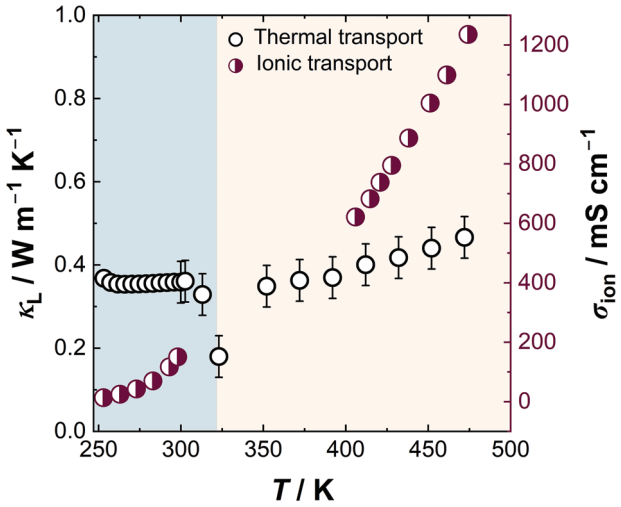


**Figure 6.** Representation of the correlation between thermal ($\kappa_L$) and ionic ($\sigma_{ion}$) transport. For ion transport data, the measurements between 253 and 298 K are our experimental data, while the high-temperature data are taken from the literature.[28] As the temperature increases, thermal transport remains almost constant, whereas ionic transport increases by orders of magnitude.

conductivity of $Cu_7PSe_6$ changes only marginally from 0.36 to 0.46 W m$^{-1}$ K$^{-1}$, reflecting a relative change of 27.8%, in the same temperature range (Figure 6). Following the high-temperature phase transition, the observed slight increase in lattice thermal conductivity might be attributed to a convection mechanism as suggested by literature,[22,39] though direct evidence is lacking in this study. This suggests that the low thermal conductivity in $Cu_7PSe_6$ is not primarily governed by the actively mobile $Cu^+$ ions, i.e., ionic conductivity, and additionally emphasizes the negligible influence of phase transitions on thermal transport in $Cu_7PSe_6$.

## 3. Conclusion

The found absence of a relationship between the ionic conductivity and thermal conductivity can be traced back to the sensitivity of both transport properties to changes to the material itself, e.g., during the phase transitions. While changes to the local atomic arrangement and connectivity between crystallographic sites have a significant impact on the diffusion of $Cu^+$, as shown by the change in the activation energy and magnitude of the ionic conductivity, the accompanied small changes to the general lattice dynamics lead to a marginal impact on the heat transport. This is further facilitated by the dominance of diffuson-type transport, which, given its local nature, is less sensitive to changes in the structure such as additional occurring point-defect scattering centers.

As there is no direct influence of ion transport on the thermal transport, it is possible to retain the sought-after low thermal conductivity, while reducing the ionic conductivity to prevent ion migration and increase stability, using an inverse of the typical design strategies from the field of solid-state ionics. Indeed, this approach was recently demonstrated for $Cu_2Se$[40] and suggested for the Ag argyrodites.[6] The present work advances the

fundamental understanding behind thermal transport in fast ionic conductors and opens possibilities for further thermoelectric design approaches.

## Supporting Information

Supporting Information is available from the Wiley Online Library or from the author.

## Acknowledgements

The research was supported by the Deutsche Forschungsgemeinschaft (DFG) under Grant Number ZE 1010/15-1 and Project Number 459785385. The authors further acknowledge the Ministry of Culture and Science of the State North Rhine Westphalia in the course of the International Graduate School of Battery Chemistry, Characterization, Analysis, Recycling and Application (BACCARA). A.A.N., J.B., and J.G. would like to acknowledge the Gauss Centre for Supercomputing e.V. (www.gausscentre.eu) for funding this project by providing generous computing time on the GCS Supercomputer SuperMUC-NG at Leibniz Supercomputing Centre (www.lrz.de) (Project No. pn73da). O.D. acknowledges funding from the US Department of Energy, Office of Science, Basic Energy Sciences, Materials Sciences, and Engineering Division, under Award No. DE-SC0019978.

Open access funding enabled and organized by Projekt DEAL.

## Conflict of Interest

The authors declare no conflict of interest.

## Data Availability Statement

Two doi for the repository are given, they will be openly available upon publication of this work.

## Keywords

$Cu^{+}$-ionic conductors, heat capacity, ionic transport, phonon density of states, structural phase transitions, thermal transport

Received: May 10, 2024
Revised: July 14, 2024
Published online:

[1] M. K. Jana, K. Biswas, *ACS Energy Lett.* **2018**, *3*, 1315.
[2] A. Basit, J. Xin, G. Murtaza, L. Wei, A. Hameed, W. Guoyu, J. Y. Dai, *EcoMat* **2023**, *5*, 12391.
[3] E. D. Wachsman, K. T. Lee, *Science* **2011**, *334*, 935.
[4] H. Liu, X. Shi, F. Xu, L. Zhang, W. Zhang, L. Chen, Q. Li, C. Uher, T. Day, G. J. Snyder, *Nat. Mater.* **2012**, *11*, 422.
[5] J. Ding, J. L. Niedziela, D. Bansal, J. Wang, X. He, A. F. May, G. Ehlers, D. L. Abernathy, A. Said, A. Alatas, Y. Ren, G. Arya, O. Delaire, *Proc. Natl. Acad. Sci. USA* **2020**, *117*, 3930.
[6] T. Bernges, R. Hanus, B. Wankmiller, K. Imasato, S. Lin, M. Ghidiu, M. Gerlitz, M. Peterlechner, S. Graham, G. Hautier, Y. Pei, M. R. Hansen, G. Wilde, G. J. Snyder, J. George, M. T. Agne, W. G. Zeier, *Adv. Energy Mater.* **2022**, *12*, 2200717.
[7] T. Böger, T. Bernges, Y. Li, P. Canepa, W. G. Zeier, *ACS Appl. Energy Mater.* **2023**, *6*, 10704.
[8] R. Hanus, J. George, M. Wood, A. Bonkowski, Y. Cheng, D. L. Abernathy, M. E. Manley, G. Hautier, G. J. Snyder, R. P. Hermann, *Mater. Today Phys.* **2021**, *18*, 100344.
[9] R. Hanus, R. Gurunathan, L. Lindsay, M. T. Agne, J. Shi, S. Graham, G. J. Snyder, *Appl. Phys. Rev.* **2021**, *8*, 031311.
[10] E. S. Toberer, A. Zevalkink, G. J. Snyder, *J. Mater. Chem.* **2011**, *21*, 15843.
[11] C. Yang, Y. Luo, X. Li, J. Cui, *RSC Adv.* **2021**, *11*, 3732.
[12] S. Lin, W. Li, S. Li, X. Zhang, Z. Chen, Y. Xu, Y. Chen, Y. Pei, *Joule* **2017**, *1*, 816.
[13] D. G. Cahill, S. K. Watson, R. O. Pohl, *Phys. Rev. B* **1992**, *46*, 6131.
[14] S. Mukhopadhyay, D. S. Parker, B. C. Sales, A. A. Puretzky, M. A. McGuire, L. Lindsay, *Science* **2018**, *360*, 1455.
[15] M. Simoncelli, N. Marzari, F. Mauri, *Phys. Rev. X* **2022**, *12*, 041011.
[16] Z. Zeng, C. Zhang, H. Yu, W. Li, Y. Pei, Y. Chen, *Mater. Today Phys.* **2021**, *21*, 100487.
[17] C. J. Hawkins, J. A. Newnham, B. Almoussawi, N. L. Gulay, S. L. Goodwin, M. Zanella, T. D. Manning, L. M. Daniels, M. S. Dyer, T. D. Veal, J. B. Claridge, M. J. Rosseinsky, *Chem. Mater.* **2024**, *36*, 4530.
[18] M. T. Agne, R. Hanus, G. J. Snyder, *Energy Environ. Sci.* **2018**, *11*, 609.
[19] Y. Xia, K. Pal, J. He, V. Ozoliņš, C. Wolverton, *Phys. Rev. Lett.* **2020**, *124*, 065901.
[20] E. Gaudin, V. Petricek, F. Boucher, F. Taulelle, M. Evain, *Acta Crystallogr., Sect. B: Struct. Sci.* **2000**, *56*, 972.
[21] E. Gaudin, F. Boucher, V. Petricek, F. Taulelle, M. Evain, *Acta Crystallogr., Sect. B: Struct. Sci.* **2000**, *56*, 402.
[22] M. K. Gupta, J. Ding, D. Bansal, D. L. Abernathy, G. Ehlers, N. C. Osti, W. G. Zeier, O. Delaire, *Adv. Energy Mater.* **2022**, *12*, 2200596.
[23] A. I. Pogodin, M. J. Filep, T. O. Malakhovska, M. Y. Sabov, V. I. Sidey, O. P. Kokhan, I. P. Studenyak, *Solid State Ionics* **2019**, *341*, 115023.
[24] A. Morscher, B. B. Duff, G. Han, L. M. Daniels, Y. Dang, M. Zanella, M. Sonni, A. Malik, M. S. Dyer, R. Chen, F. Blanc, J. B. Claridge, M. J. Rosseinsky, *J. Am. Chem. Soc.* **2022**, *144*, 22178.
[25] J. Hong, O. Delaire, *Mater. Today Phys.* **2019**, *10*, 100093.
[26] S. Adams, R. P. Rao, *Bond Valences*, (Eds.: I. D. Brown, K. R. Poeppelmeier), Springer, Berlin, Germany **2014**.
[27] C. Shi, X. Xi, Z. Hou, E. Liu, W. Wang, J. Chen, G. Wu, *Solid State Ionics* **2017**, *300*, 182.
[28] R. Chen, P. Qiu, B. Jiang, P. Hu, Y. Zhang, J. Yang, D. Ren, X. Shi, L. Chen, *J. Mater. Chem. A* **2018**, *6*, 6493.
[29] M. K. Gupta, J. Ding, N. C. Osti, D. L. Abernathy, W. Arnold, H. Wang, Z. Hood, O. Delaire, *Energy Environ. Sci.* **2021**, *14*, 6554.
[30] J. L. Niedziela, D. Bansal, A. F. May, J. Ding, T. Lanigan-Atkins, G. Ehlers, D. L. Abernathy, A. Said, O. Delaire, *Nat. Phys.* **2019**, *15*, 73.
[31] S. Muy, R. Schlem, Y. Shao-Horn, W. G. Zeier, *Adv. Energy Mater.* **2021**, *11*, 2002787.
[32] K. A. Graeser, J. E. Patterson, J. A. Zeitler, T. Rades, *Pharmaceutics* **2010**, *2*, 224.
[33] M. T. Agne, K. Imasato, S. Anand, K. Lee, S. K. Bux, A. Zevalkink, A. J. E. Rettie, D. Y. Chung, M. G. Kanatzidis, G. J. Snyder, *Mater. Today Phys.* **2018**, *6*, 83.
[34] H. Yu, L.-C. Chen, H.-J. Pang, P.-F. Qiu, Q. Peng, X.-J. Chen, *Phys. Rev. B* **2022**, *105*, 245204.
[35] A. Yadav, P. Deshmukh, K. Roberts, N. Jisrawi, S. Valluri, *J. Phys. Commun.* **2019**, *3*, 105001.
[36] L. J. Sham, J. M. Ziman, *Solid State Phys.* **1963**, *15*, 221.
[37] Y. M. Beltukov, V. I. Kozub, D. A. Parshin, *Phys. Rev. B* **2013**, *87*, 134203.
[38] T. Bernges, M. Peterlechner, G. Wilde, M. T. Agne, W. G. Zeier, *Mater. Today Phys.* **2023**, *35*, 101107.
[39] Q. Ren, M. K. Gupta, M. Jin, J. Ding, J. Wu, Z. Chen, S. Lin, O. Fabelo, J. A. Rodríguez-Velamazán, M. Kofu, K. Nakajima, M. Wolf, F. Zhu, J. Wang, Z. Cheng, G. Wang, X. Tong, Y. Pei, O. Delaire, J. Ma, *Nat. Mater.* **2023**, *22*, 999.
[40] B. Trawiński, *J. Mater. Sci.* **2023**, *58*, 17034.